Golay-Coded Excitations for Rotational Intravascular Ultrasound Imaging

TAEWON CHOI[1], (Member, IEEE), SEOYUN CHANG[1], TAE-HYUNG KIM[1], (Member, IEEE), AND JINHYOUNG PARK[1,2], (Member, IEEE)

[1]Department of Biomedical Engineering, Sungkyunkwan University, Suwon 16419, South Korea
[2]Biomedical Institute for Convergence, Sungkyunkwan University, Suwon 16419, South Korea

Corresponding author: Jinhyoung Park (jin.park@skku.edu)

ABSTRACT Intravascular ultrasound (IVUS) imaging employs high imaging frequencies (from 20 to 60 MHz) to visualize microvascular structures by sacrificing the depth of penetration with an increased signal attenuation. To compensate for the reduced echo signal-to-noise ratio, chirp-coded excitations, which require complex system configurations in high-frequency ultrasound imaging, are considered as suitable methods for rotational IVUS. Golay-coded excitations, which only need simple electronics and have no range sidelobe artifacts if the incident locations of the Golay pair are the same, have not been considered for rotational IVUS. In this study, computer simulations and experiments with a custom-made IVUS imaging system running at 30 fps are performed to investigate on the optimal operational conditions of Golay-coded excitations in rotational IVUS imaging. While the code length was not a significant factor affecting the range sidelobe level (RSLL), a change in the imaging frequency from 25 MHz to 66 MHz increased the RSLL from -65 dB to -45 dB with 2048 beamlines. In addition, an increase in the number of beamlines from 64 to 2048 reduced the RSLL from -17 dB to -50 dB in the simulation and from -14 dB dB to -38 dB in the experiment. To further decrease the RSLL, a weighted averaging method that compressed the coded pulse was proposed. The RSLL could be suppressed from -50 dB to -80 dB and from -38 dB to -53 dB in the simulation and experiment, respectively. Golay-coded excitation imaging was also successfully demonstrated on freshly harvested pig coronary arteries.

INDEX TERMS Intravascular ultrasound, Golay-coded excitation, range sidelobe level, weighted averaging, high-frequency ultrasound.

I. INTRODUCTION

Intravascular ultrasound (IVUS) imaging employs high imaging frequencies greater than 20 MHz to visualize microstructures (e.g., calcium caps, intima, and media layers) within blood vessels. Because a higher imaging frequency with the shorter pulse width results in a better spatial resolution which enables discriminating each layers among those small structures at a resolution of approximately tens of microns, numerous efforts to increase the imaging frequencies up to 60 MHz have recently been made [1]–[3]. The improvement in spatial resolution sacrifices the depth of penetration, thus limiting the field of view in IVUS imaging because

of exponentially increased signal attenuation as the imaging frequency increases [4], [5].

With the degradation in image quality, entire structures of diseased vessels, including heavy plaque burdens, may not be identified, and physicians may have trouble measuring the vessel size and choosing the right type of stent [6], [7]. Previously, the chirp-coded excitation, a frequency-modulated signal, was proposed to recover the reduced depth of penetration in high-frequency ultrasound imaging [8]. Because the chirp coded excitation signal can be compressed to a short burst by convolving the chirp with its matched filter, a time-reversed transmitted waveform, the visible range can be expanded without decreasing the spatial resolution.

In rotational IVUS imaging, chirp-coded excitations have been demonstrated to better show structures over a diseased site than single-cycle excitations. Although chirp-coded

---

The associate editor coordinating the review of this article and approving it for publication was Mohammad Zia Ur Rahman.

excitations have the advantage of requiring single transmissions in compressing the echo signal over that of other methods, the method requires combinations of an arbitrary waveform generator and a broadband power amplifier that increase the system's complexity to have comparable performances with the single-cycle excitations [4], [9], [10]. In addition, the method creates inherent range sidelobes that degrade the image quality. While the inherent range sidelobe levels (RSLLs) can be reduced by multiplying a window function to the chirp burst [9], axial resolution must be lowered to accommodate a reduced bandwidth. By contrast, a Golay-coded excitation, transmitting a phase-modulated waveform, requires only switching bipolar or unipolar pulse generators, which most ultrasound imaging systems are adopting. A Golay code can be perfectly compressed by applying corresponding matched filters to two beamlines of a Golay pair and accumulating these two filtered outputs. Because the range sidelobes of two matched filtered outputs are completely complementary when the two beamlines are acquired from the same position, the range sidelobes completely disappear after the accumulation [11]–[14].

However, Golay-coded excitation has been suggested as an inappropriate solution for a mechanically scanning ultrasound imaging system because the continuous mechanical translations in scanning objects result in acquiring two beam lines of a Golay pair from different positions and increasing the RSLLs and decreasing the dynamic ranges [15]. Because the transducer typically rotates at a high speed of 1800 rotations per minute (rpm) in a rotational IVUS, the quality of compression of the Golay-coded excitations is dependent on pulse repetition rates, which are related to the number of scanlines, Golay code length, and imaging frequencies. Previously, the back-to-back transmission of orthogonal code sets was proposed to achieve the code compression by a single transmission in communications applications [11], [16]. However, the use of elongated pulses may limit visibility in the near field where important clinical information, e.g. thin calcium cap, intima layer, stent deployed, in IVUS imaging needs to be visualized.

This study investigates the optimizations of imaging parameters in applying Golay-coded excitation to rotational IVUS imaging. Furthermore, a novel compression algorithm is proposed to further enhance image quality under the presence of high rotational speeds (1800 rpm) with a commercially available IVUS catheter for the first time. The effects of rotational translations on degradable imaging factors: increased RSLLs, decreased echo signal-to-noise ratio (eSNR), and spatial resolutions, are investigated by running Field II [17], [18] simulations for the different imaging parameters of code lengths, numbers of scanlines, and imaging frequencies.

For the experimental optimizations, the simulation results are validated by using a custom-made real-time coded excitation IVUS imaging system and a commercial IVUS catheter, which closely mimics commercial IVUS operations. Instead of rotating imaging targets at slow speeds [7], the custom-made system spins the transducer at 1800 rpm with Golay-coded transmissions at a pulse repetition frequency of 68 kHz. This enables an assessment of the feasibility of applying Golay codes to rotational IVUS imaging for the first time.

With the optimized custom-made system, wire and tissue phantoms are measured to quantify the effects of mechanical translations on image qualities. In addition, freshly harvested pig coronary arteries with a bare metal stent deployed are imaged to demonstrate the performance of Golay-coded excitations with the optimized parameters and the proposed compression algorithm under a high rotational speed. The image performance achieved with this set-up is also compared with that using chirp-coded excitations.

II. THEORY OF OPERATION

While a perfect correlation can be achieved by transmitting two codes to the same position of a stationary imaging object, a rotational IVUS scanner continuously translates incident positions, and a mismatch between the two codes that triggers range sidelobe artifacts and lowers the eSNR is unavoidable. The increase in the RSLL caused by the mismatch of the Golay pair can be analyzed by considering either amplitude mismatches or phase aberrations between the two echo signals. The typical Golay transmit waveform having a center frequency of f can be defined as follows [11]:

$$G_{tx1}(t) = G_1(t)e^{j2\pi ft}, \quad G_{tx2}(t) = G_2(t)e^{j2\pi ft} \quad (1)$$

where G_{tx1} and G_{tx2} are the transmitted Golay pair, and G_1 and G_2 are the binary Golay pair. The impulse response of a point target located at a depth of d_i is written as:

$$h(t, d_i) = k(d_i) \cdot \delta(t - d_i/c) \quad (2)$$

where k, δ, and c are attenuation incorporated with depth, impulse response, and the speed of sound, respectively. The received echo signal is roughly estimated by the convolution of the impulse response and the transmit burst as written in the following equations.

$$G_{rx1}(t) = G_1(t - \tau 0) \cdot e^{j2\pi f(t-\tau 0)},$$
$$G_{rx2}(t) = G_2(t - \tau 0) \cdot e^{j2\pi f(t-\tau 0)} \quad (3)$$

where G_{tx1} and G_{tx2} are the transmitted Golay pair, and $\tau 0$ is d_i/c. For a stationary imaging target with two N bit codes transmitted from the same position, the following equation need to be satisfied.

$$G_{rx1}(t) * G_{tx1}(-t) + G_{rx2}(t) * G_{tx2}(-t) = 2N\delta(t - \tau 0) \quad (4)$$

where $G_{txx}(-t)$ is the time reversed form of $G_{txx}(t)$. In case of having different amplitude between $G_{rx1}(t)$ and $G_{rx2}(t)$, the output in the equation (4) cannot be a Dirac-delta function, and range sidelobes are generated. Also, range sidelobes can be generated when d_i between two echo signals are different due to the continuous position change in the rotational IVUS.

Figure 1 shows pulse sequences for IVUS Golay-coded excitation imaging. Four beamlines are formed by alternately
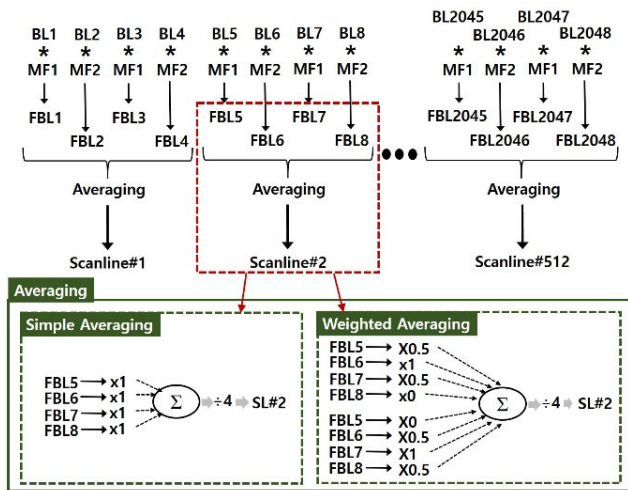
FIGURE 1. Beam sequence of Golay-coded excitations implemented in custom-designed rotational IVUS system. Two block diagrams at bottom provide details of averaging blocks within red dashed box on top. Simple averaging method and weighted averaging method are depicted on left and right of two bottom block diagrams, respectively. BLx, MF1, MF1, FBLx, and "∗" are xth beamline, one of Golay matched filter pair, other of Golay matched filter pair, xth matched-filtered beamline, and convolution function, respectively.

transmitting the Golay pair, and a corresponding matched filter is convolved with each beamline. The averaging of the four beamlines follows, completing the code compression and forming a scanline. Instead of using two beamlines for a scanline, four beamlines are chosen to enhance the SNR and reduce the distance between beamlines.

A beamline in this paper indicates an A-line acquisition by a transmission, and a scanline indicates a final A-line processed possibly by multiple beamlines before scan conversion. Because the maximum number of beamlines presented in powers of two allowing at least a 20 mm field of view with 30fps is 2048, and the typical number of scanlines is 512, the accumulation of more than four beamlines was not considered.

A. AMPLITUDE MISMATCH
Amplitude mismatches between two beamlines of a Golay pair occur when the pairs are acquired from different positions with different echogenicities. When the amplitudes of two beamlines are different, the range sidelobes from the two beamlines after the matched filter is applied are no longer complementary and still remain after the accumulation of these filtered beamlines. Under these circumstances, a pair of imaging beams needs to be transmitted within at least half a beam width in order to reduce the difference in amplitudes.

The beam width of an ultrasound transducer is the same as the lateral resolution defined by a product of the f-number and wavelength. For a typical flat IVUS transducer having an aperture size of approximately 500 μm and an imaging frequency of 40 MHz, its natural focus is 1.6 mm. This results in an f-number of 2.9 and an estimated lateral resolution

of 112 μm. Note that the rotational center is assumed to be 500 μm before the transducer's surface owing to the thickness of the backing materials. The angle corresponding to half the lateral resolution is 1.4°, which can be approximately calculated by half the beam width over the distance from the rotational center to the focal point.

Therefore, Golay beamlines forming a scanline need to be completed within a rotation of 1.4°, and the minimum number of scanlines having correlations between a Golay pair is 240. Assuming that a typical number of scanlines is defined by a power of two, the minimum number of scanlines is 256, and 1024 beamlines are needed with the pulsing sequence as shown in Figure 1. In the far field out of the focal point, the beam width is also broadened with a radiation angle of ±1.4° calculated by equation (5) [5].

$$\Phi = \sin^{-1}(0.61(\lambda/a)) \qquad (5)$$

where Φ, λ, and a are the beam diverging angle, wavelength, and aperture size of the transducer.

B. PHASE ABERRATION
The amount of phase shift caused by the time-of-flight differences between the beamlines in the Golay pair may generate range sidelobes. The phase shift is induced by either mechanically moving the transducers or moving the targets because the rotational scanners change their incidental positions at every beamline, or the imaging targets translate their positions between two transmissions. For a rotational IVUS scanner, an unfocused 40-MHz transducer with a 500-μm aperture size is typically used.

$$d2 = \sqrt{(b^2 + (b + d1)^2 - 2b(b + d1)\cos\theta)}$$
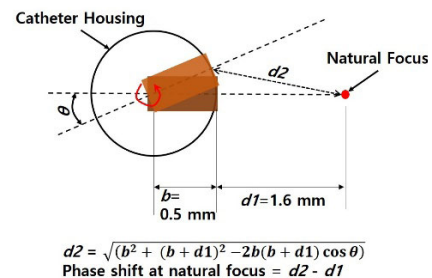Phase shift at natural focus = d2 - d1

FIGURE 2. Method to calculate amount of phase shift (d2 - d1) at focal distance of d1 with transducer within catheter having diameter of 1 mm when transducer is translated by θ.

The natural focus of the transducer is approximately 1.6 mm where typical coronary vessel layers and stent struts are located. The amount of phase shift between the two beamlines at 1.6 mm is 3.2, 0.8, 0.2, and 0.05 μm for 64, 128, 256, and 512 beamlines per frame, respectively. Figure 2 describes how the amount of phase shift indicated by d2 is calculated when the transducer rotates by the angle θ. Because a typical sampling rate for an IVUS system is approximately 200 MHz, corresponding to a distance of 3.85 μm between samples, the amount of a phase aberration is less than the distance between the two sample points.

Therefore, phase aberrations affect the RSLLs less than the amplitude mismatch because the amount of phase aberration with 512 scanlines meeting the half a beam width between the Golay pair is only 0.07 μm. This is insignificant compared to the errors caused by the sampling frequency.

C. COMPENSATION STRATEGY

As shown in Figure 1, the concept of a weighted averaging method is implemented to suppress the RSLL. Owing to the continuous incident position changes in the rotational IVUS, the current beamline is correlated not only with the previous beamline but also with the next beamline. As the number of beamlines is increased and the space between them is reduced, the correlations with both neighbored beamlines are increased.

Therefore, to reduce the amplitude mismatches between the two beamlines of a Golay pair, three consecutive beamlines are used to compress the Golay code instead of using a pair of beamlines. The central beamline among the three and average of neighboring beamlines becomes a Golay pair. For example, a second beamline is accumulated with the average of the first and the third beamline. For this reason, at least three beamlines need to be transmitted within the half of the beam width. For the weighted averaging of four beamlines, the weighting values are [0.5, 1.5, 1.5, 0.5] as a result of the sum of [0.5, 1, 0.5, 0] and [0, 0.5, 1, 0.5]. By contrast, a simple averaging uses the same weighting values of [1, 1, 1, 1].
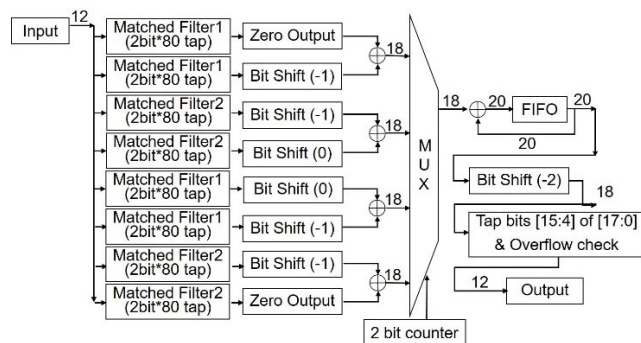

FIGURE 3. An example of a hardware block diagram which may be implemented by programming a field programmable gated array. The block diagram is designed for 16 bit Golay pulse compression with the weighted averaging method, and the number on each arrow between blocks is number of bit of data. First-In-First-Out (FIFO) buffer ultimately generates an output of the pulse compression.

The Golay code compression with the weighted averaging can be implemented in a real time hardware although off-line Matlab based program was used in this study. Figure 3 shows an example of a hardware functional block diagram for a 16-bit Golay code compression with the weighted averaging method. The convolution in Figure 1 can be replaced by the matched filter block which uses an 80 tap corresponding Golay waveform with a 200 MHz sampling rate. The weighting values are the same as the values shown in Figure 1. 'Zero output' makes the output to zero, and 'Bit shift (−1)' does divide a binary value by 2. The First-In-First-Out (FIFO)

buffer ultimately generates an output of accumulating four weighted beamlines, and the bit shift of −2 is for dividing the output by 4 to complete the averaging function. After truncating the useable data bit, the output of the code compression is generated. Because the entire process is designed for binary numbers, the proposing block diagram can be implemented in a field programmable gate array (FPGA).

III. METHOD

A. FIELD II SIMULATION

The effects of mechanical movements on the Golay pulse compression were simulated by modeling rotational IVUS imaging with a Field II program. An unfocused piston-type single-element flat transducer with an aperture size of 500 μm and a bandwidth of 55% was modeled and located at the origin in the simulation field. A numerical phantom with wire targets located every 0.5 mm from the surface of the transducer to 3 mm in depth was created. Note that the phantom was composed of single 1s for wires and 0s for the background.

The phantom was rotated around a rotational center 500 μm behind the origin of the transducer's surface to mimic the mechanical rotation considering the thickness of the backing material of the IVUS transducer instead of the translating transducer's position. A "transmit" and "receive" was completed at every step angle of the rotation, i.e., 2π divided by the number of beamlines. For the Golay-coded excitation, a Golay pair was alternatively transmitted, and the code was compressed by convolving a matched filter and summing the convolved echo signals of the filtered Golay pair.

The RSLL caused by the mechanical translation was investigated as a function of the number of scanlines, number of Golay bits, and imaging frequencies. The sampling rate was 200 MHz, and the field of view was 6 mm. The total number of beamlines was 64, 128, 256, 512, 1024, and 2048 for obtaining 16, 32, 64, 128, 256, and 512 scanlines, respectively. Single scanlines were processed by averaging four beamlines. From the final processed images, the RSLL dependencies on the frequency, code length, number of beamlines, and different weighting values shown in the theory section were investigated.

The improvement in eSNR defined by the formula below [19] with Golay-coded excitations was also simulated by mixing random noises with the simulated raw data before the pulse compression. The amplitude of the random noise was adjusted to achieve an eSNR of 30 dB before pulse compression in the wire target studies.

$$eSNR = 20\log_{10}\left(\frac{Max\ Echo\ signal\ level}{Standard\ Deviation\ of\ noise}\right) \quad (6)$$

B. EXPERIMENTAL SETUP

A commercial IVUS catheter (Revolution, Philips, Amsterdam, Netherlands) was employed for the experimental measurements. From pulse echo studies, the bandwidth of the

transducer was 26%, and the center frequency was 42 MHz. Experiments were performed by using a custom-made four-channel high-frequency ultrasound transceiver. The transmit part of the transceiver was composed of three stages: pulse waveform generator, waveform driver, and high-voltage switching amplifier.

The transmitted signal was generated by programming the waveform using two complex programmable logic devices (CPLDs) with a clock frequency of 160 MHz. For generating bipolar transmit signals, positive and negative pulses were generated from separate channels in CPLDs (XC9572XL, Xilinx, San Jose, CA, USA) and were placed into the input of a metal–oxide–semiconductor field-effect transistor (MOSFET) driver (ISL55110, Renesas, Tokyo, Japan). Note that the negative portion of the waveform was generated later by half transmit wavelength than the positive portion generation for conforming bipolar signals. The two waveforms of Golay pair were programmed in CPLD and alternately transmitted at every rising edge of the tx trigger signal shown in Figure 4. The pulse repetition frequency for having 2048 beamlines in 30 fps was 61.44 kHz, and one waveform in the code pair was transmitted in 30.72kHz.
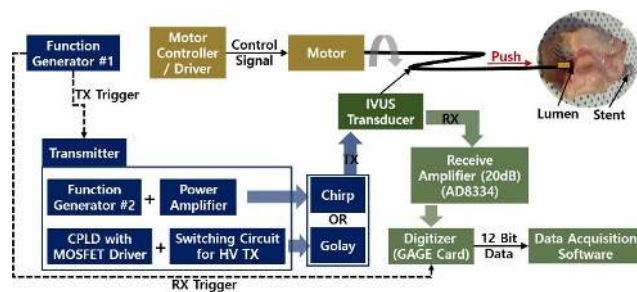

FIGURE 4. Block diagram of the experimental wire target imaging system.

The amplified signals were fed to a switching-circuit configuration composed of two N-MOSFETs (TC6215, Microchips, Chandler, AZ, USA) to generate high-voltage transmit signals having amplitudes of 60 V_{pp}. The outputs for the positive and negative portions of the two MOSFETs become inputs to a center-tapped 1:1 transformer (78613/4JC, Murata Power Solutions, Kyoto, Japan) to generate bipolar transmit signals with only a positive power supply.

The transmit signal passed through an expander that connected two diodes (PMBD7000, Nexperia, Nijmegen, Netherlands) in parallel with opposite directions. The echo signal passed through a shunt voltage limiter of two reversely connected diodes in parallel and was amplified by 29 dB with a low-noise amplifier (AD8334, Analog Devices, Norwood, MA, USA). The analog output was filtered out with a custom-made 5$^{\text{th}}$-order Butterworth bandpass filter [21] having a −3-dB bandwidth from 15 MHz to 53 MHz. The amplified signal was sent to a 12-bit digitizer (CS121G2, Gage, Lockport, IL, USA) and saved for postprocessing using the MATLAB program (R2013a, Mathworks, Inc., Natick, MA, USA).

Post-processing included high-pass filtering for direct current offset rejection, matched filter application, log compression, and scan conversion to form a circular shape. The RSLL was investigated for a 16-bit, 40-MHz Golay code. A Golay pair was alternately transmitted at a pulse repetition frequency (PRF) of 61.44 kHz to obtain 2048 beamlines per frame and four beamlines per scanline. The rotational scanning speed was 1800 rpm to achieve 30 fps. Control signals for a brushless motor (EC-max 16, Maxon Motor, Sachseln, Switzland) were generated by a control board (Mega2560, Arduino, Somerville, MA, USA) and amplified by a motor driver in order to move the motor. A commercial IVUS catheter was connected.

After flushing the catheter with water, a wire phantom, tissue-mimicking phantom, and pig coronary arteries with a metal stent deployed were scanned. For a comparison with the performance of Golay-coded excitations, a Hanning-windowed 1-μm-long chirp signal sweeping from 20 MHz to 60 MHz was created based on the following formula [23]:

$$Chirp(t) = cos\left[2\pi(fi + \frac{(fo - fi)\,t}{2CL})\right] \quad (7)$$

where *fi* and *fo* are the start and end frequencies of the modulations, respectively, and *CL* is the code length. In the experiment, *fo* and *fi* were 60 MHz and 20 MHz, respectively, and the code length was 1 μm. The chirp signal was loaded on a bench-top waveform generator (AFG3252, Tektronics, Beaverton, OR, USA) with an arbitrary waveform mode. The output signal became an input to a power amplifier (350L, ENI, Rochester, NY, USA) to generate transmit signals with 60 V_{pp}. A system block diagram showing the overall operation is shown in Figure 4.
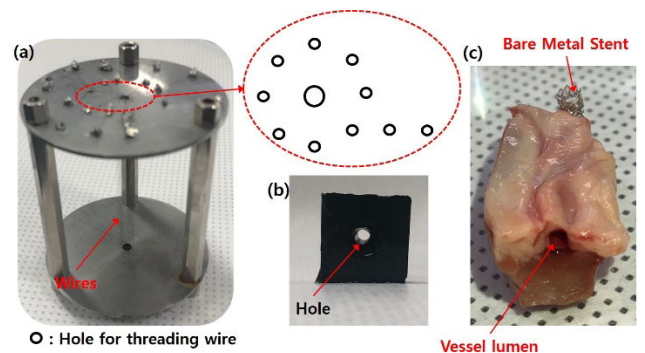

FIGURE 5. Phantom structures of (a) wire phantom and (b) tissue-mimicking phantom. (c) Freshly harvested pig coronary artery with stent deployed.

C. PHANTOM PREPARATION

Two stainless-steel disks, 5 cm in diameter and 1 mm in thickness, were placed in parallel with three 5-cm pillar spacers located at the edge of the disk. A circular hole with a diameter of 1.2 mm was created in the center of the stainless-steel disk to introduce the IVUS catheter into the phantom. Eight holes with a diameter of 0.2 mm were machined along

equally spaced circumferential locations of a concentric circle with the disk center, and two more holes were fabricated along the radial direction outside the concentric circle shown in Figure 5(a). Tungsten wires with a diameter of 50 μm were threaded between the two disks and fixed on the disk by welding for visualizing the cross section of the wire phantom with side-looking rotational scanners.

The tissue-mimicking phantom was fabricated by mixing acrylamide solution with graphite powder. After degassing the solution for 30 min, ammonium persulfate and N,N,N',N'-tetramethylethylenediamine (TEMED) were added to the mixed solution, and the solution was stirred quickly [22]. The solution was left at room temperature until it gelatinized. A block of a cubic centimeter was separated from the gelatinized solution, and a hole of about 3 mm in diameter was made in the center of the gel cube by using a 3-mm drill bit, as shown in Figure 5(b).

D. EX-VIVO SAMPLE PREPARATION
A left anterior descending (LAD) coronary artery was harvested from a fresh pig heart, as shown in Figure 5(c). A bare metal stent (BMS) was deployed from the middle to the end of the blood vessel by expanding the balloon at a pressure level of 6 atm. Clots were created by leaving blood samples at room temperature for 4 h. These clots were inserted into the prepared vessel to simulate clot- or blood-filled lumen. The IVUS catheter was pushed into the vessel lumen for acquiring images of both native vessels and the stented region within the artery.
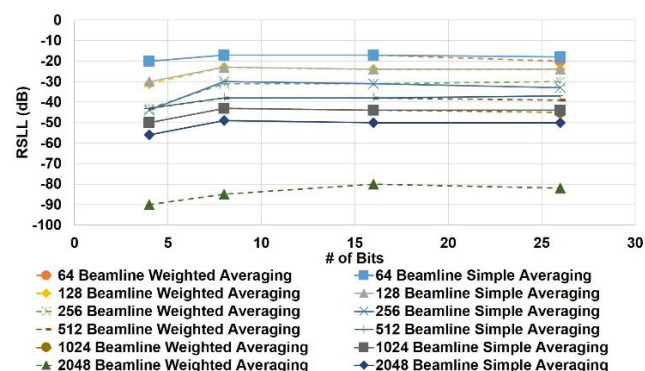
FIGURE 6. RSLL vs. code length. Solid lines and dashed lines are simple averaging method and weighted averaging method, respectively.

IV. RESULTS
A. NUMBER OF BITS VS. RANGE SIDELOBE LEVEL
Figure 6 shows the RSLLs dependent on the code length and number of beamlines. As the number of bits increased, the RSLL slightly increased by a few decibels from 8 bits to 26 bits. There was a significant increase in the RSLL by 6–7 dB from 4 bits to 8 bits. The dashed lines represent RSLL curves for weighted averaging, and the solid lines for normal averaging.

For both averaging methods, the code length was not a significant cause of the increased RSLL compared to the number of beamlines. The RSLL is displayed for different numbers

of beamlines from 64 to 2048. The increase in the number of beamlines reduced the RSLL from −18 dB with 64 beamlines to −45 dB with 2048 beamlines when utilizing a simple averaging method. By contrast, the weighted averaging method resulted in nearly the same RSLL up to 1024 beamlines except for 2048 beamlines, in which the RSLL noticeably decreased by 36 dB with the 16-bit Golay code in the simulation.

B. IMAGING FREQUENCY VS. RANGE SIDELOBE LEVEL
The effects of the imaging frequency on the RSLLs are presented in Figure 7. As the frequency increased from 25 MHz to 66 MHz, the RSLL increased using the simple averaging method. While the RSLL increased by 25 dB from −37 dB to −12 dB with 64 beamlines, it increased by 21 dB with 2048 beamlines, from −65 dB to −44 dB. The amount of RSLL reduction as the number of beamlines increased by a power of two was approximately 6 dB.
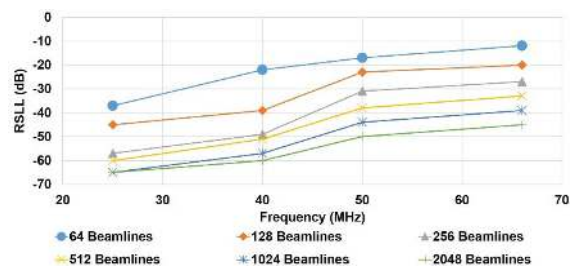
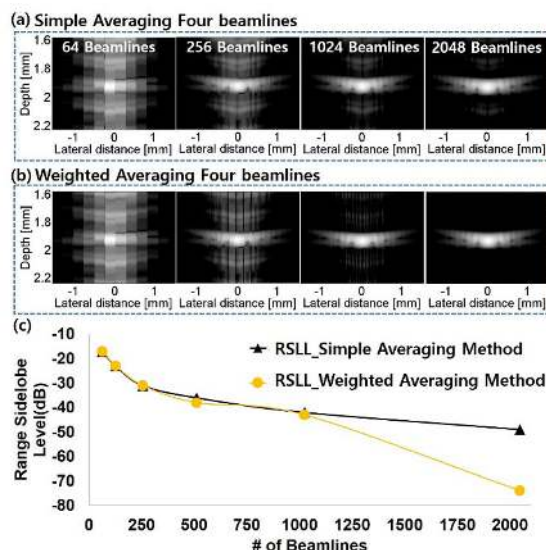**FIGURE 7.** Simulation results showing RSLL vs. imaging frequency.

FIGURE 8. Simulation results showing wire targets at natural focus using (a) normal averaging method and (b) weighted averaging method. (c) RSLL vs. number of beamlines. RSLLs were measured for 64, 128, 256, 512, 1024, and 2048 beamlines. Triangles and circles indicate results obtained using normal and weighted averaging methods, respectively.

C. NUMBER OF BEAMLINES VS. RANGE SIDELOBE LEVEL
Figure 8 shows the simulation results, demonstrating that the RSLL decreased as the number of beamlines increased. Figure 8(a) shows closeup images at a natural focus using the

simple averaging method in the 60-dB dynamic range, and Figure 8(b) shows the corresponding images for the weighted averaging method. Figure 8(c) shows the maximum RSLL measured using the normal averaging and weighted averaging methods indicated with triangles and circles, respectively.

Using the simple averaging method, the range sidelobes above and below the main lobe became fainter as the number of beamlines increased but were still visible with the use of 2048 beamlines. However, the range sidelobes completely disappeared by using the weighted averaging method with 2048 beamlines. As the graph in Figure 8(c) shows, the range sidelobe was suppressed down to −80 dB by using the weighted averaging method with 2048 beamlines, while the RSLL stayed at −50 dB with the simple averaging method. Although the maximum RSLLs in the images with simple and weighted averaging were similar, the regions where the range sidelobes exist were smaller with the weighted averaging method than with the simple averaging method.

Figure 9 shows the experimental results of demonstrating the wire target images in the 55-dB dynamic range for different numbers of beamlines and the corresponding RSLLs. Figure 9(a) shows the wire target images acquired by using the simple averaging method for different numbers of beamlines (BL in the figure), and Figure 9(b) shows the same using the weighted averaging method. The white arrows in the images indicate the range sidelobe artifacts visualized in the 55-dB dynamic range. From 64 to 1024 beamlines, the range side lobes for both compression methods are clearly identified, while the weighted averaging method shows fainter range sidelobes.

With 1024 beamlines, the RSLL using the weighted averaging method dropped by 13 dB compared to the simple averaging method. Using the simple averaging method, the range sidelobes can be identified up to 2048 beamlines, but these are barely visualized at 2048 beamlines using the weighted averaging method. Figure 9(c) compares the echo brightness profiles between simple and weighted average method. The profiles were harvested along the dotted-white lines marked in Figures 9(a) and 9(b) for the simple and weighted averaging methods, respectively. Noise and peak levels for the same number of beamlines were quite similar each other, while eSNR with 128 beamlines is 6 dB lower than the one with 2048 beamlines and RSLLs were also reduced by 13 dB and 32 dB for the simple and the weighted averaging approaches, respectively. With 2048 beamlines, RSL was disappeared by using the weighted averaging method. In contrast to the simulation method, the RSLL with 2048 beamlines dropped down to −53 dB, limited by the eSNR of the experimental images. The measured eSNR were also enhanced as the number of beamlines increased. In Figure 9(d), the lines with circles and squares represent the eSNR changes with the function of the number of beamlines.

Note that the y-axis in Figure 9 is shared with the RSLL, and the eSNR takes only the absolute value of the axis. The eSNR sharply increased by 13 dB as the number of beamlines changed from 64 to 256 and almost linearly increased as
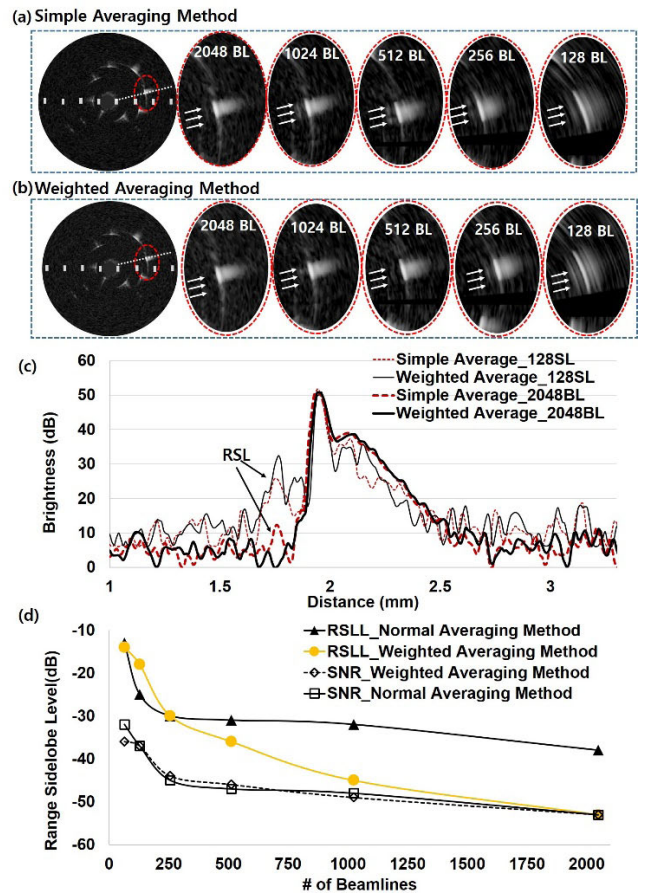

FIGURE 9. Experimental results showing wire targets using (a) a simple averaging method and (b) a weighted averaging method. (c) The brightness profiles along the dotted white line in (a) and (b) are plotted with thicker dashed red and solid black lines, respectively, for 2048 beamlines, and thinner dashed red and solid black lines, respectively, for 128 beamlines. RSL in the figure means range sidelobe. (d) RSLL and SNR vs. number of beamlines. RSLLs were measured for 64, 128, 256, 512, 1024, and 2048 beamlines. Triangles and circles indicate simple and weighted averaging methods, and squares and diamonds represent eSNRs for simple and weighted averaging methods, respectively.

the number of beamlines changed from 256 to 2048. With 2048 beamlines, an eSNR of 53 dB was achieved for both the simple and weighted averaging methods.

D. CODE LENGTH VS. ESNR AND SPATIAL RESOLUTION

With a 40-MHz Golay-coded excitation and 2048 beamlines, the eSNR improved by 11, 12, 16, and 18 dB for 4-, 8-, 16-, and 26-bit code lengths, respectively, as the simulation study shows. In the experimental wire target studies shown in Figure 10, eSNR also improved for 4-, 8-, 16-bit code lengths by 6, 12, and 22 dB, respectively.

Axial resolutions decreased slightly with the use of Golay codes from 51 μm to 54 μm, but barely changed as the code length was elongated. The lateral resolution noticeably decreased from 197 μm to 264 μm, as shown in Figure 10(a)–10(d).
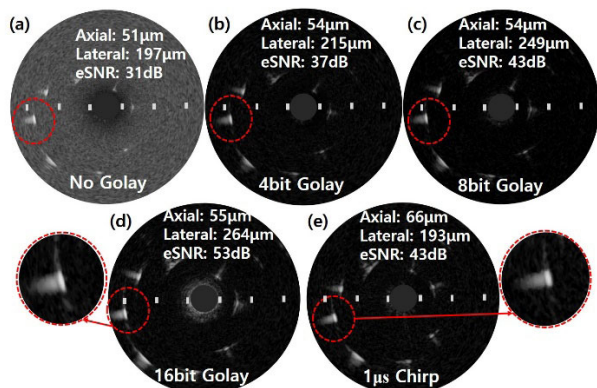
FIGURE 10. Wire target images acquired by (a) single-cycle pulse, (b) 4-bit Golay code, (c) 8-bit Golay code, (d) 16-bit Golay code, and (e) 1-μm-long Hanning-windowed chirp-coded excitations. All images are 6-mm field of view, and graticules are marked at every 1 mm in image.

The use of chirp-coded excitation presented effects of eSNR enhancement by 12 dB similar to those with an 8-bit Golay code. Compared with Golay-coded excitations, the axial resolution with a chirp-coded excitation decreased from 55 to 66 μm. However, the lateral resolution was maintained compared with the single-cycle pulse transmission. In the magnified wire target images shown to the sides of Figure 10(d) and 10(e), the thickness of the wire target with a 16-bit Golay code was thinner than that with chirp-coded excitations, while the shape was laterally broader with Golay than chirp-coded excitations even if the code length of the chirp was longer than that of the 16-bit Golay.
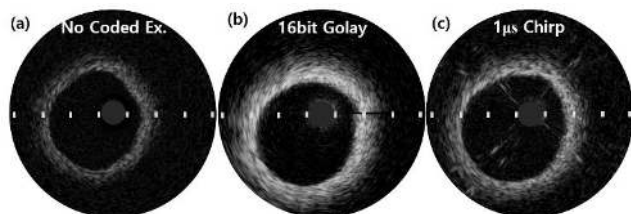

FIGURE 11. Tissue-mimicking phantom images acquired by (a) single-cycle pulse, (b) 16-bit Golay code, and (c) 1-μm-long Hanning-windowed chirp-coded excitations. All images have a 7-mm field of view, and graticules are marked every 1 mm in the image.

E. TISSUE PHANTOM STUDIES

Figure 11 compares IVUS images acquired by a single-cycle pulse, 16-bit Golay excitations, and chirp-coded excitations from the custom-made tissue-mimicking phantom. The measured diameter was between 3 and 4 mm. The measured depth of penetration [23] was 0.8, 1.5, and 1.0 mm for single-cycle, Golay, and chirp pulses, respectively. The image with the Golay code had better contrast in the tissue region than the other imaging methods. The lumen boundary with chirp seemed to be clearer than the Golay-coded excitations owing to the laterally broadened speckle patterns.

F. EX-VIVO STUDIES WITH PIG CORONARY ARTERIES

Figure 12 presents cross-section images of freshly harvested pig coronary arteries. Figures 12(a) and (b) were
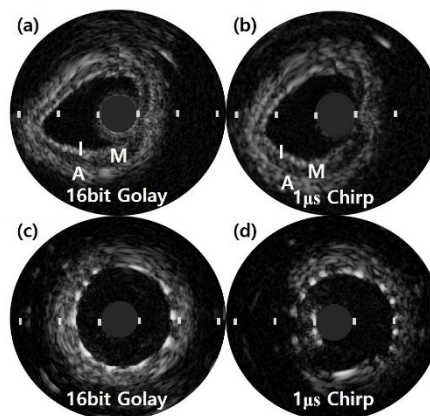

FIGURE 12. IVUS images of pig native coronary arteries acquired by (a) 16-bit Golay code and (b) 1-μm-long Hanning-windowed chirp-coded excitations, and stented coronary arteries acquired by (c) 16-bit Golay code and (d) 1-μm-long Hanning-windowed chirp-coded excitations. All images have 5.5-mm field of view, and graticules are marked every 1 mm in each image. In image, letters of I, M, and A indicate intima, media, and adventitia layers, respectively.

both acquired from a native vessel by 16-bit Golay and chirp-coded excitations, respectively. In both images, vessel layer structures of intima (I), media (M), and adventitia (A) were clearly identified, while the intima layers depicted in Figure 12(a) with Golay looked thinner than those of the chirp image. Peripheral structures of vessels in the 12 o'clock direction were identified with the Golay code but barely showed with the chirp-coded excitation. Figures 12(c) and (d) show stented vessel images with the 16-bit Golay and chirp-coded excitations, respectively. The stent was well apposed with the lumen without showing any space between the vessel walls and struts. While all the struts were spatially resolved well in both images, struts in the chirp image looked better separated than in the Golay image, while the struts in the Golay image were better resolved along the radial direction.

Figure 13 compares images acquired by using 16-bit Golay-coded excitations with the simple and weighted averaging methods from stented vessels filled with water [Figure 13(a) and (b)] and blood clots [Figures 13(c) and (d)]. All images were processed with 2048 beamlines. While the range sidelobes from the metal struts and a strong echo reflector (indicated by white arrows) were clearly visualized with the simple averaging method in Figure 13(a), these artifacts were barely identified in Figure 13(b) when acquired by the weighted averaging method.

With the lumen was filled with clots, range sidelobe artifacts were still identified from the strong echo signals, as indicated by the solid white arrows in Figure 13(c), while no such artifacts could be observed in Figures 13(d) and (e) when the 16-bit Golay code with the weighted averaging method and chirp-coded excitation were used, respectively. The region of broadened speckle patterns where nonuniform rotation distortion (NURD) is presumed is marked with a white dashed circle in Figures 13(c)–(e). Another type of range sidelobe artifacts indicated by the white dotted arrows
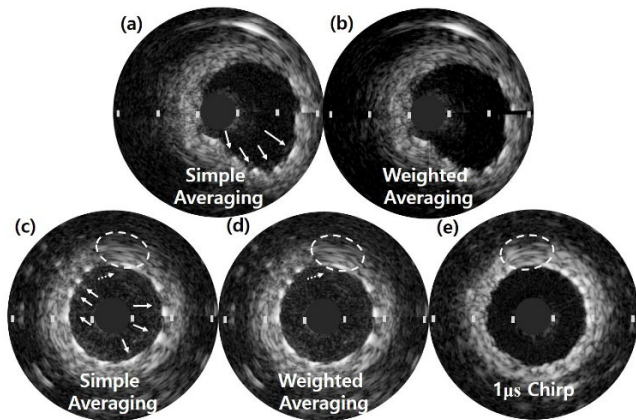
FIGURE 13. IVUS images of stented pig coronary arteries with water-filled lumen acquired by 16-bit Golay code with (a) simple averaging and (b) weighted averaging methods. Stented vessel filled with clots are imaged with 16-bit Golay code with (c) simple averaging and (b) weighted averaging methods. (e) Water-filled stented vessel is scanned by using chirp-coded excitation. White dashed circles indicate distorted regions possibly caused by nonuniform mechanical rotation, and white dotted arrows indicate range sidelobe artifacts caused by these nonuniform rotational operations.

was identified right above the NURD region with the Golay-coded excitations, while a clear lumen region was acquired by the chirp-coded excitation, as shown in Figure 13(e).

V. DISCUSSION

Previously, the use of Golay-coded excitation was not considered for a rotational IVUS. However, it can share existing switching pulse generators for single-cycle bursts without changing the fundamental hardware and transducer designs because of the inherently lowered pulse compression qualities caused by the discrepancy between two consecutive echo signals acquired by the Golay pair. Instead, chirp-coded excitations have been demonstrated as feasible for increasing the eSNR in a rotational IVUS imaging system even if the complex electronics for arbitrary waveform generation and power amplifiers are prerequisites for implementing high-frequency (20–60 MHz) chirp-coded excitations [21].

In addition, as previous studies showed, the RSLL is inherently generated without applying windowing functions to the transmit pulses, which causes a reduced bandwidth and lowered axial resolutions. In the current wire phantom study demonstrated in Figure 10(e), the axial resolution was lowered by 20% owing to the Hanning windowing function; this probably narrowed the transducer's bandwidth to less than 30%. Because typical commercially available transducers have narrow bandwidths of less than 50%, the applications of the chirp signal to IVUS may be unable to achieve decent performance for the eSNR and spatial resolutions, as Figures 10–12 demonstrate.

In the current study, the effects of the frequency, Golay code length, and number of beamlines on the RSLL, eSNR, and spatial resolutions were investigated to determine the optimal imaging parameters for minimizing the image defects

caused by the continuous mechanical translations. The imaging parameters were loaded on the custom-made IVUS imaging system, which produced realistic imaging performance with high rotational speed and a commercially available catheter.

As demonstrated by the results of the simulations and experiments, increasing the number of beamlines from 64 to 2048 effectively reduced the RSLL by 33 dB in the simulations and 39 dB in the experimental wire-target studies. The eSNR was also enhanced by 22 dB, as shown in Figure 9(c) of the experimental results. With the use of 2048 beamlines per imaging frame, the range sidelobe artifacts still remained, and the eSNR needed to be improved to visualize the stent struts and vessel layers clearly. As Figure 13 shows, the range sidelobe artifacts were still identified by a simple averaging of the Golay pair even in the presence of blood within the lumen while images acquired by chirp-coded excitation do not have such artifacts.

In the analytical analysis, the reason for increasing the RSLL was mostly amplitude mismatches rather than the phase shift, which might only affect the near field where the amount of phase shift in the two beamlines of the Golay pair from the same imaging target in the near field increased by the transducer's positional translation. As shown in Figure 8(a), range sidelobes were still generated at a depth of approximately 1.9 mm, where the phase mismatch was nearly trivial although the beam intensity along the lateral direction rapidly changed.

Because imaging frequency is directly related to the lateral beam size the RSLL is sensitive to changes in the imaging frequency. In the simulation, an increase in the imaging frequency from 25 MHz to 66 MHz increased the RSLLs up to 25 dB. The measured lateral resolution at 40 MHz was 290 μm, whereas it was 244 μm and 157 μm at 50 MHz and 66 MHz, respectively. The narrower beams generated a higher RSLL.

Similar physics apply to the number of beamlines. Figure 8(c) and Figure 9(c) show decreases in the RSLL as the number of beamlines increased and the space between the two echoes of the Golay pair decreased.

The code length did not significantly change the RSLL except for a change of approximately 6 dB from 4 bit to 8 bit, as shown in Figure 5. In both the simulations and experiments, 2048 beamlines at 40 MHz and a 16-bit Golay code demonstrated the best performance in RSLL reduction.

Despite of the efforts to reduce RSLLs by increasing the number of beamlines, the RSLL remained at −50 dB in the simulation and −38 dB in the experiment. This can be visualized in the typical imaging dynamic range of an IVUS, e.g., 50–60 dB. To further suppress the RSLL, a weighted averaging method that uses a beamline and the average value of its two neighboring scanlines significantly reduced the RSLL by more than 25 dB in the simulation. When compressing the Golay code with four alternating Golay sequences, a weighting value of [0.5, 1.5, 1.5, 0.5] was applied to four

consecutive beamlines, and the discrepancy in the amplitude between the Golay pair was considerably reduced.

While the RSLL dramatically decreased at 2048 beamlines in the simulation, experimental studies showed that an improved RSLL of no less than −53 dB because it was limited by the eSNR of the real imaging system. The noise level was further reduced by optimizing the power regulators or integrating all systems in a ground plane. The NURD in the motor rotation could increase the RSLL, as Figures 13(c) and (d) show, even if the weighted averaging method was utilized because of uneven incident positions among the four beamlines forming a scanline as shown in Figure 1. In future work, NURD artifacts could be detected by monitoring motor position signals, and the artifacts could be reduced by changing the weighting values.

In Figures 10–13, comparisons of imaging performances between Golay and chirp-coded excitations are presented. As the wire target studies indicate, Golay-coded excitations showed better axial resolutions, while the lateral resolutions of chirp imaging were better than those of the Golay-coded excitations. In the tissue-mimicking phantom images, the lumen boundaries of chirp-coded excitation were clearer than in the images with Golay-coded excitation, and the stent struts were better isolated laterally with chirp-coded excitation. However, the Golay-code imaging visualized the vessel layers better with its higher axial resolution than the chirp-coded imaging method. In addition, Golay-coded imaging may better visualize malapposed stent struts since apposed stent struts are effectively displayed using the Golay code in Figure 12(c).

The feasibility of using Golay-coded excitation in IVUS was successfully demonstrated for the first time with a high-frame-rate custom-made IVUS imaging system and a commercial IVUS catheter. All things considered, the current study showed that Golay-coded excitation imaging with more than 2048 beamlines and the weighted averaging method can achieve comparable or even better image qualities with the eSNR and spatial resolutions than chirp-coded excitations. Range sidelobe artifacts can also be minimized by using the weighted averaging method. The representative three vessel layers were clearly identified in the native vessel, and the apposition of stent struts was effectively visualized.

VI. CONCLUSION

The application of Golay-coded excitation, which requires relatively simple hardware configurations, to rotational IVUS imaging was investigated by using a commercially available IVUS catheter and a custom-made high-frame-rate imaging system. The number of beamlines and imaging frequencies are the critical factors for minimizing RSLLs; the code length related to the SNR was not a significant factor in suppressing the RSLL. In compressing the Golay code, a weighted averaging method was necessarily considered to further decrease RSLLs for rotational IVUS imaging because there was limited enhancement with an increase in the number of beamlines and when using the simple averaging method.

Given these considerations, the feasibility of using Golay-coded excitation with IVUS was presented by successfully visualizing microstructures of coronary vessel layers and stent struts although further experiments on a larger group of vessel types may be needed to confirm the clinical relevance of the proposing method.

REFERENCES

[1] K. Okada, H. Kitahara, Y. Mitsutake, S. Tanaka, T. Kimura, P. G. Yock, P. J. Fitzgerald, F. Ikeno, and Y. Honda, "Assessment of bioresorbable scaffold with a novel high-definition 60 MHz IVUS imaging system: Comparison with 40-MHz IVUS referenced to optical coherence tomography," *Catheter Cardiovasc Intervent*, vol. 91, no. 5, pp. 874–883, 2018.

[2] J. Yuan, S. Rhee, and X. N. Jiang, "60 MHz PMN-PT based 1-3 composite transducer for IVUS imaging," in *Proc. IEEE Ultrason. Symp.*, Nov. 2008, pp. 682–685.

[3] T. Ma, M. Yu, Z. Chen, C. Fei, K. K. Shung, and Q. Zhou, "Multi-frequency intravascular ultrasound (IVUS) imaging," *IEEE Trans. Ultrason., Ferroelectr., Freq. Control*, vol. 62, no. 1, pp. 97–107, Jan. 2015.

[4] J. Mamou, J. A. Ketterling, and R. H. Silverman, "Chirp-coded excitation imaging with a high-frequency ultrasound annular array," *IEEE Trans. Ultrason., Ferroelectr., Freq. Control*, vol. 55, no. 2, pp. 508–513, Feb. 2008.

[5] K. K. Shung, *Diagnostic Ultrasound: Imaging and Blood Flow Measurements*. Boca Raton, FL, USA: CRC Press, 2006.

[6] J. Aoki, A. C. Abizaid, P. W. Serruys, A. T. L. Ong, E. Boersma, J. E. Sousa, and N. Bruining, "Evaluation of four-year coronary artery response after sirolimus-eluting stent implantation using serial quantitative intravascular ultrasound and computer-assisted grayscale value analysis for plaque composition in event-free patients," *J. Amer. College Cardiol.*, vol. 46, pp. 1670–1676, Nov. 2005.

[7] W. Qiu, X. Wang, Y. Chen, Q. Fu, M. Su, L. Zhang, J. Xia, J. Dai, Y. Zhang, and H. Zheng, "Modulated excitation imaging system for intravascular ultrasound," *IEEE Trans. Biomed. Eng.*, vol. 64, no. 8, pp. 1935–1942, Aug. 2017.

[8] D. Maresca, K. Jansen, G. Renaud, G. van Soest, X. Li, Q. Zhou, N. de Jong, K. K. Shung, and A. F. W. van der Steen, "Intravascular ultrasound chirp imaging," *Appl. Phys. Lett.*, vol. 100, no. 4, 2012, Art. no. 043703.

[9] J. Park, C. Hu, and K. K. Shung, "Stand-alone front-end system for high- frequency, high-frame-rate coded excitation ultrasonic imaging," *IEEE Trans. Ultrason., Ferroelectr., Freq. Control*, vol. 58, no. 12, pp. 2620–2630, Dec. 2011.

[10] C. Passmann and H. Ermert, "A 100-MHz ultrasound imaging system for dermatologic and ophthalmologic diagnostics," *IEEE Trans. Ultrason., Ferroelectr., Freq. Control*, vol. 43, no. 4, pp. 545–552, Jul. 1996.

[11] C. Jin, S.-P. Chen, Z.-D. Qin, and T.-F. Wang, "A new scheme of coded ultrasound using Golay codes," *J. Zhejiang Univ. Sci. C*, vol. 11, no. 6, pp. 476–480, 2010.

[12] X. Su, "An investigation of binary coded excitation methods using golay code pairs for high frequency ultrasound imaging," M.S. thesis, Dept. Elect. Comput. Eng., Ryerson Univ., Toronto, ON, Canada, 2004.

[13] R. Y. Chiao and X. Hao, "Coded excitation for diagnostic ultrasound: A system developer's perspective," *IEEE Trans. Ultrason., Ferroelectr., Freq. Control*, vol. 52, no. 2, pp. 160–170, Feb. 2005.

[14] T. Misaridis and J. A. Jensen, "Use of modulated excitation signals in medical ultrasound. Part II: Design and performance for medical imaging applications," *IEEE Trans. Ultrason., Ferroelectr., Freq. Control*, vol. 52, no. 2, pp. 192–207, Feb. 2005.

[15] J. Park and P. D. Corl, "Systems and methods for producing an image from a rotational intravascular ultrasound device," U.S. Patent 20 140 276 063 A1, Sep. 18, 2014.

[16] A. T. Fam and R. Kadlimatti, "Good code sets from complementary pairs via polyphase chips," in *Proc. IEEE Mil. Commun. Conf.*, Nov. 2016, pp. 952–957.

[17] J. A. Jensen, "FIELD: A program for simulating ultrasound systems," in *Proc. IEEE 10th Nordic-Baltic Conf. Biomed. Imag.*, vol. 4. Mar. 1996, pp. 351–353.

[18] J. A. Jensen and N. B. Svendsen, "Calculation of pressure fields from arbitrarily shaped, apodized, and excited ultrasound transducers," *IEEE Trans. Ultrason., Ferroelectr., Freq. Control*, vol. 39, no. 2, pp. 262–267, Mar. 1992.

[19] N. Q. Nguyen and R. W. Prager, "High-resolution ultrasound imaging with unified pixel-based beamforming," *IEEE Trans. Med. Imag.*, vol. 35, no. 1, pp. 98–108, Jan. 2016.

[20] A. H. Al-Khalidi, M. E. Lewis, J. N. Townened, R. S. Bonser, and J. H. Coote, "A novel and simple technique to allow detection of the position of the R-waves from intraventricular pressure waveforms: Application to the conductance catheter method," *IEEE Trans. Biomed. Eng.*, vol. 48, no. 5, pp. 606–610, May 2001.

[21] M. R. Bosisio, J.-M. Hasquenoph, L. Sandrin, P. Laugier, S. L. Bridal, and S. Yon, "Real-time chirp-coded imaging with a programmable ultrasound biomicroscope," *IEEE Trans. Biomed. Eng.*, vol. 57, no. 3, pp. 654–664, Mar. 2010.

[22] T. Ling, Q. Jin, H. Yao, and H. Zheng, "Design and characterization of a tissue-mimicking phantom for ultrasonic elastography," in *Proc. 4th Int. Conf. Bioinf. Biomed. Eng. (ICBBE)*, Jun. 2010, pp. 1–4.

[23] Y. Li, J. Ma, K. H. Martin, M. Yu, T. Ma, P. A. Dayton, X. Jiang, K. K. Shung, Q. Zhou, "An integrated system for superharmonic contrast-enhanced ultrasound imaging: Design and intravascular phantom imaging study," *IEEE Trans. Biomed. Eng.*, vol. 63, no. 9, pp. 1933–1943, Sep. 2016.

TAE-HYUNG KIM (M'18) was born in Suwon, South Korea, in 1992. He received the B.S. degree in physics from Sungkyunkwan University, Suwon, South Korea, in 2018, where he is currently pursuing the integrated Ph.D. degree with the Department of Biomedical Engineering. His research interests include the hardware design of printed circuit boards and the design of field programmable gate array (FPGA) programs for developing high-frequency ultrasound imaging systems.

TAEWON CHOI (M'18) received the B.S. degree in biomedical engineering from Inje University, Gimhae, South Korea, in 2018. He is currently pursuing the integrated M.S./Ph.D. degree in biomedical engineering with Sungkyunkwan University, Suwon, South Korea. His research interests include the development of novel intravascular ultrasound (IVUS) imaging instruments with high performance and efficiency using a new material that has distinguished piezoelectric properties, and creative ultrasonic transmission technologies that enable more accurate diagnosis and imaging for targeted lesions.

SEOYUN CHANG was born in Suwon, South Korea, in 1997. She is currently pursuing the B.S. degree in biomedical engineering from Sungkyunkwan University, Suwon, South Korea. Her research interests include hardware and software design for ultrasound elastography, and intravascular ultrasound imaging. She is currently designing a high-frequency ultrasound pulse generator and receiver by designing both analog and digital circuits.

JINHYOUNG PARK (M'18) was born in Busan, South Korea, in 1975. He received the B.S. degree in astronomy and the M.S. degree in biomedical engineering from Seoul National University, Seoul, South Korea, in 2002 and 2004, respectively, and the Ph.D. degree in biomedical engineering from the University of Southern California, Los Angeles, CA, USA, in 2011. From 2004 to 2008, he was a Principal Engineer with the SIEMENS Ultrasound Group, South Korea. He was a Postdoctoral Research Associate with the Department of Biomedical Engineering, University of Southern California, in 2012, and a Senior Engineer with Volcano Corporation, Rancho Cordova, CA, USA (which was acquired by Philips, in 2015), from 2013 to 2016. Since 2016, he has been an Assistant Professor with the Biomedical Engineering Department, Sungkyunkwan University, Suwon, South Korea. He also has expertise in algorithms for interventional flow measurement. He is the author of 20 peer-reviewed articles. He holds three patents. His research interest includes the fabrication of ultrasound systems and transducers applied to intravascular ultrasound imaging and noninvasive neuro modulations.

• • •